An Empirical Normal Mode Diagnostic Algorithm Applied to NCEP Reanalyses

AYRTON ZADRA

Department of Atmospheric and Oceanic Studies, McGill University, Montreal, Quebec, Canada

GILBERT BRUNET

Department of Atmospheric and Oceanic Studies, McGill University, Montreal, and Recherche en Prévision en Numérique, Environment Canada, Dorval, Quebec, Canada

JACQUES DEROME

Department of Atmospheric and Oceanic Studies, McGill University, Montreal, Quebec, Canada

(Manuscript received 15 March 2001, in final form 8 April 2002)

ABSTRACT

A diagnostic algorithm, based on the empirical normal mode decomposition technique, is proposed as a diagnostic tool in studies of the atmospheric variability. It begins by analyzing the transient eddies in terms of empirical modes that are orthogonal with respect to wave activities. Time-dependent amplitudes together with wave activity spectra are used to classify the modes and compute their propagation properties.

The algorithm is applied to a sequence of four Northern Hemisphere winters taken from the National Centers for Environmental Prediction reanalyses, with a focus on the upper troposphere and lower stratosphere, giving a set of empirical modes of wind, pressure, specific volume, and potential vorticity. Results indicate that most of the wave activity is carried by large-scale, eastward-propagating modes centered at middle and high latitudes. Some properties of the leading modes, such as their average phase speeds, are in good agreement with the predictions of linear dynamics.

Characteristics of the leading wavenumber-5 mode, such as its dipolar pressure pattern near the summer hemisphere tropopause, its propagation speed of 12 m s^{-1} and decay rate of 3 days, can be explained by the theory of quasi modes, defined as superpositions of singular modes sharply peaked in the phase speed domain. Other large-scale, midlatitude modes also show properties compatible with the quasi-modal description, suggesting that quasi modes play an important role in the upper-troposphere dynamics.

1. Introduction

The decomposition of data in terms of orthogonal basis functions is a useful tool in studies of the variability of atmospheric fields. Different sets of basis functions and the associated scalar product have different advantages: for instance, one set may be suitable in statistical studies, while another set can more promptly reveal the dynamical properties of the field components. The latter is the kind of basis functions we are interested in and we propose, here, a method to construct one such set. The purpose of this paper is therefore twofold: first, to describe a diagnostic algorithm based on the idea of normal mode decomposition and designed for studies of atmospheric variability; second, to illustrate the various features of the algorithm by applying it to a set of analyzed data.

The algorithm is essentially a three-dimensional extension of the empirical normal mode (ENM) technique previously used by Brunet and Vautard (1996) in studies of two-dimensional shallow water models on the sphere. The architecture of the ENM method is similar to that used to find empirical orthogonal functions (EOFs), except that EOFs are based on the statistical notion of variance whereas ENMs make use of wave activities.

It has been suggested by Andrews (1983a) and others that wave activities and the associated conservation relations can be useful in the diagnosis and interpretation of propagating disturbances. For instance, Held (1985) studied the barotropic decay of perturbations on the sphere, using the orthogonality of neutral modes with respect to wave activities to decompose initial disturbances and separate discrete modes from singular

Corresponding author address: Dr. Ayrton Zadra, Division de Recherche en Prévision en Numérique, Environment Canada, Floor 5e, 2121 Route Transcanadienne, Dorval, QC H9P 1J3, Canada.
E-mail: Ayrton.Zadra@ec.gc.ca

modes. Killworth and McIntyre (1985) applied nonlinear wave activity conservation to the problem of nonlinear Rossby wave critical-layer problem and showed that wave-breaking regions behave as reflectors. Magnusdottir and Haynes (1998) also used nonlinear wave activity diagnostics to study low-latitude reflection of quasi-stationary Rossby waves excited by midlatitude topography, thus extending the results obtained with a shallow water model by Brunet and Haynes (1996).

In the context of the ENM theory, waves activities have been used by Brunet (1994) to analyze the discrete and continuous spectra of modes propagating on the 315-K isentrope. Using data generated by numerical experiments in a shallow water model on the sphere, Brunet and Vautard (1996) have shown that ENMs, constructed with the appropriate choice of basic state and the corresponding wave activity, have a more monochromatic behavior and thus provide better predictions than those obtained with EOFs in statistical linear models. Charron and Brunet (1999) used the conservation law of pseudoenergy to decompose model data into ENMs and to study the generation, propagation, and breaking of inertia gravity waves excited by mountains and by nonlinear effects near the jet stream.

Here, the ENM algorithm is applied to winter data taken from the National Centers for Environmental Prediction (NCEP) reanalyses [In this paper, ''winter'' refers to winter in the Northern Hemisphere, that is, December–January–February (DJF).] The diagnosis is focused on transient eddies propagating in a subdomain of the atmosphere, namely the upper-tropospheric and lower-stratospheric regions. The output consists of a complete set of winter ENMs, describing the atmospheric variability in those regions. Modes are accompanied by spectra of wave activity, kinetic energy, available potential energy, enstrophy, and zonal phase speeds. We choose to work in isentropic coordinates for which the algorithm's design seems to assume its simplest form.

Results confirm that in the upper troposphere and lower stratosphere most wave activity is found in large-scale eastward-propagating ENMs. Despite the effects of nonlinearity and forcing, the average frequency calculated from the power spectrum of some of the leading modes is in good agreement with the frequency predicted by the linear theory. This property was previously observed in weakly nonlinear experiments with a shallow water model (Brunet and Vautard 1996) and an interpretation based on stochastic modeling was proposed by Charron and Brunet (1999).

Among large-scale ENMs we find evidence of propagating quasi modes organized around the tropopause. The notion of quasi modes has been proposed by Rivest et al. (1992) and Rivest and Farrell (1992) as a paradigm for synoptic-scale waves in the midlatitude upper troposphere, where the presence of strictly positive gradients of potential vorticity implies that the upper-edge Eady problem (Eady 1949) has no modal solutions (Green 1960); only singular modes are admitted. Quasi modes are superpositions of these singular modes and Rivest et al. (1992) have shown that they can be generated on realistic timescales and provide a consistent description of synoptic waves near the jet stream. Here we will argue that larger-scale modes, such as the leading zonal wavenumber-5 ENM, also show spatial patterns, phase speeds, and decay rates compatible with those predicted by the theory of midlatitude quasi modes. In particular, the baroclinic nature of the wavenumber-5 mode in the summer Southern Hemisphere had already been observed in previous studies (Lambert 1986; Chen et al. 1987; Lin and Chan 1989) and the ENM analysis indicates that this mode can be more accurately described as a quasi mode.

The ENM algorithm also provides detailed spectra of wave activities, including amplitudes of kinetic and available potential energy of each mode, from which we can measure properties such as energy partition and spectral slopes of inertial ranges. These properties are supposed to characterize large-scale turbulence in the atmosphere (Charney 1971) and where previous studies (see, e.g., Boer and Shepherd 1983) have used Fourier modes or spherical harmonics, the ENM method uses normal modes for flow decomposition.

This paper is structured as follows: in section 2 we present a brief review of the ENM theory and the usage of wave activities; section 3 explains the methodology of the diagnostic algorithm; section 4 gives a description of the dataset, and the main results are then discussed in section 5; conclusions are summarized in the last section.

2. ENM theory revisited

A brief review of ENM theory, focusing on the similarities to EOF analysis, is presented below. More details may be found in Brunet (1994), Brunet and Vautard (1996), Charron and Brunet, (1999) and Zadra (2000).

Let us represent the atmospheric state by $\boldsymbol{\psi}$, a multicomponent field including, for example, wind speed, density and pressure fields. Subtracting the time-mean state $\overline{\boldsymbol{\psi}}$, we define the anomaly field $\boldsymbol{\psi}'$, which is further decomposed in terms of a biorthogonal basis $\{a_n(t), \psi_n(\mathbf{r})\}$ as follows:

$$\boldsymbol{\psi}(t, \mathbf{r}) = \overline{\boldsymbol{\psi}} + \boldsymbol{\psi}', \qquad \overline{\boldsymbol{\psi}}(\mathbf{r}) = \frac{1}{\Delta t}\int_{t_0}^{t_0+\Delta t} \boldsymbol{\psi}\, dt, \quad (1)$$

$$\boldsymbol{\psi}'(t, \mathbf{r}) = \sum_n a_n(t)\psi_n(\mathbf{r}) + \boldsymbol{\epsilon}(t, \mathbf{r}), \quad (2)$$

$$(a_m a_n) = \overline{a_m(t)a_n(t)} = \delta_{mn}, \quad (3)$$

$$\langle \psi_m | \psi_n \rangle = \int \psi_m^{\mathrm{T}}(\mathbf{r})\mathbf{G}(\mathbf{r})\psi_n(\mathbf{r})\, d\mathbf{r} = \lambda_m \delta_{mn}, \quad (4)$$

where t is time; the overbar indicates time average over the interval $[t_0, t_0 + \Delta t]$; $\mathbf{r}$ is the vector of spatial co-

ordinates; $\boldsymbol{\epsilon}$ is the decomposition error; $\{a_n\}$ is a set of uncorrelated, normalized, time-dependent amplitudes; $\mathbf{G}$ is a chosen metric; $\{\psi_n\}$ is a set of basis functions, orthogonal with respect to $\mathbf{G}$; δ_{mn} is the Kronecker's delta; the upper index T indicates transposition; $\int d\mathbf{r}$ is an integral over the spatial domain; and λ_m is the squared norm of the mth basis function.

The basis functions are chosen to minimize the mean-square error $\overline{\langle \boldsymbol{\epsilon} \mid \boldsymbol{\epsilon} \rangle}$, which leads to two alternative eigenvalue problems:

$$\begin{aligned} M\psi_n &= \lambda_n \psi_n, \\ M\psi_n(r_1) &= \int \mathbf{C}(\mathbf{r}_1, \mathbf{r}_2)\mathbf{G}(\mathbf{r}_2)\psi_n(\mathbf{r}_2)\, d\mathbf{r}_2, \\ \lambda_n a_n &= \langle \psi_n \mid \boldsymbol{\psi}' \rangle, \quad \text{or} \\ Wa_n &= \lambda_n a_n, \\ Wa_n(t_1) &= \int_{t_0}^{t_0+T} \tau(t_1, t_2) a_n(t_2)\, \frac{dt_2}{T}, \end{aligned} \tag{5}$$

$$\psi_n = (a_n \boldsymbol{\psi}'). \tag{6}$$

Above, $\mathbf{C}(\mathbf{r}_1, \mathbf{r}_2) = \overline{\boldsymbol{\psi}'(t, \mathbf{r}_1)\boldsymbol{\psi}'^{\mathrm{T}}(t, \mathbf{r}_2)}$ and $\tau(t_1, t_2) = \langle \boldsymbol{\psi}'(t_1, \mathbf{r}) \mid \boldsymbol{\psi}'(t_2, \mathbf{r}) \rangle$ represent the anomaly covariances in space and time. The above equations provide two equivalent approaches to the construction of the biorthogonal set $\{a_n, \psi_n\}$. In practice, since both time and space are often discretized and the operators $\mathbf{C}$, τ become square matrices, it is more convenient to solve the eigenvalue problem with the smaller matrix. The time-covariance approach is sometimes called the snapshot method (Sirovich and Everson 1992).

So far, the metric has been left as a builder's choice. Choosing a Euclidian metric, say $\mathbf{G} = 1$, leads to the well-known EOF method, where ψ_n is an EOF, a_n the corresponding principal component (PC), and λ_n measures the partial variance captured by ψ_n. On the other hand, the ENM method uses a metric derived from conservation laws of linear dynamics: assuming the existence of a quadratic wave activity $Q = \int \boldsymbol{\psi}'(t, \mathbf{r})^{\mathrm{T}} G_Q(\mathbf{r}) \boldsymbol{\psi}'(t, \mathbf{r})\, d\mathbf{r}$—conserved in time to leading order in the amplitude of disturbances $\boldsymbol{\psi}'$, in the absence of forcing and damping—it can be shown (Held 1985) that the normal modes of the linearized system are orthogonal with respect to $\mathbf{G}_Q$ and that the wave activity Q is a sum of modal contributions. Choosing the wave activity metric $\mathbf{G}_Q(\mathbf{r})$, the eigenvectors of (5) are called ENMs, the amplitudes a_n are still named PCs, but the eigenvalues λ_n are interpreted as amounts of wave activity.

When the linear theory holds or is a good approximation, ENMs tend to true normal modes with monochromatic PCs. If nonlinearities are present, the set of ENMs still provides a basis for data decomposition whose physical significance was first pointed out by Brunet (1994). Nonlinearities, dissipation, and forcing may eventually be accommodated in the ENM method: when these effects admit a simple stochastic modeling, Charron and Brunet (1999) have shown that the spatial structure of a normal mode is preserved and the associated frequency, as predicted by the linear theory, is given by its power-spectrum mean frequency.

3. Methodology

a. Dynamics and wave activities in isentropic coordinates

Primitive equations and conservation laws are known to assume their simplest form in isentropic coordinates (see, e.g., Andrews 1983b). In the upper troposphere and lower stratosphere, potential temperature is a well-behaved vertical coordinate. For all these reasons, the diagnostic algorithm has been designed to analyze atmospheric fields in θ coordinates. To set notation, the dry hydrostatic primitive equations and some useful formulæ are listed below:

$$\frac{\partial u}{\partial t} + \frac{1}{a\cos\phi}\frac{\partial}{\partial \lambda}\left[\frac{1}{2}(u^2 + v^2) + M\right] - \zeta v = F_1 - \dot{\theta}\frac{\partial u}{\partial \theta}, \tag{7}$$

$$\frac{\partial v}{\partial t} + \frac{1}{a}\frac{\partial}{\partial \phi}\left[\frac{1}{2}(u^2 + v^2) + M\right] + \zeta u = F_2 - \dot{\theta}\frac{\partial v}{\partial \theta}, \tag{8}$$

$$\begin{aligned} \zeta &= f + \frac{1}{a\cos\phi}\left(\frac{\partial v}{\partial \lambda} - \frac{\partial}{\partial \phi}(u\cos\phi)\right), \\ f &= 2\Omega \sin\phi, \end{aligned} \tag{9}$$

$$\frac{\partial \sigma}{\partial t} + \frac{1}{a\cos\phi}\left[\frac{\partial}{\partial \lambda}(\sigma u) + \frac{\partial}{\partial \phi}(\sigma v \cos\phi)\right] = -\frac{\partial}{\partial \theta}(\sigma\dot{\theta}), \tag{10}$$

$$\frac{\partial p}{\partial \theta} = -g\sigma, \qquad \frac{\partial M}{\partial \theta} = c_p\left(\frac{p}{p_r}\right)^{\kappa}, \tag{11}$$

where (λ, ϕ, θ) represent longitude, latitude, and potential temperature respectively; a is the earth's radius; (u, v) are horizontal wind components; $M = c_p T + gz$ is the Montgomery streamfunction; $\dot{\theta}$ is the diabatic heating rate; (F_1, F_2) is the body force per unit mass; ζ is the vertical component of absolute vorticity; Ω is the earth's rotation rate; σ is the density defined such that σdV is the mass of the volume element $dV = a^2 \cos\phi d\lambda d\phi d\theta$; potential vorticity (PV) is denoted by $q = \zeta/\sigma$; g is the gravity constant; $p_r = 1000$ hPa; $\kappa = R/c_p$; R is the gas constant; and c_p the specific heat at constant pressure for dry air.

The unforced, conservative limit corresponds to vanishing F_1, F_2, and $\dot{\theta}$. In the linearized limit, conservation of wave activities is related to symmetries of the basic state. Time independence of the basic state leads to the conservation of pseudoenergy (Andrews 1983a; Haynes 1988) while zonal symmetry gives conservation of pseudomomentum (Held 1985). In the case of multiple symmetries, normal modes are orthogonal with respect to all wave activities (Haynes 1988; McIntyre and Shepherd 1987) simultaneously.

Hereafter we shall consider time-independent zonally symmetric basic states, with fields—labeled by a ''zero'' index—that obey the following balance conditions:

$$\frac{\partial}{\partial\theta}\left[\left(f + \frac{u_0 \tan\phi}{a}\right)u_0\right] = -\frac{1}{a}\frac{\partial}{\partial\phi}\left[c_p\left(\frac{p_0}{p_r}\right)^{\kappa}\right], \quad (12)$$

$$v_0 = 0, \qquad \frac{\partial p_0}{\partial\theta} = -g\sigma_0, \qquad q_0 = \frac{\zeta_0}{\sigma_0}. \quad (13)$$

In θ coordinates, the pseudomomentum density reads:

$$J = \cos\phi\left(\sigma' u' - \frac{\sigma_0^2}{2\gamma_0}q'^2\right), \qquad \gamma_0 = \frac{1}{a}\frac{\partial q_0}{\partial\phi}, \quad (14)$$

where primed variables denote departures from the basic state. The first term is the usual wave momentum, whereas the second is an enstrophy-like contribution coming from wave-mean field interactions. The pseudoenergy density is

$$A = E + u_0\frac{J}{\cos\phi},$$
$$E = \frac{\sigma_0}{2}(u'^2 + v'^2) + \frac{\lambda}{2}p_0^{-k}p'^2, \quad (15)$$

with $\lambda = R/(gp_r^{\kappa})$ and $k = 1 - \kappa = c_v/c_p$. The first two components of the energy density E correspond to the wave kinetic energy, and the third represents the available potential energy. The last term in A is sometimes called Doppler term, as explained below.

When zonal symmetry holds, we may construct normal modes ψ_{ns} with fixed zonal wavenumber s. Here, n is just a label used to distinguish modes with the same wavenumber s. If ω_{ns} is the normal mode frequency, a zonal phase speed $c_{ns} = \omega_{ns}/(s\ a^{-1})$ may be defined and the mode's pseudoenergy A_{ns} and pseudomomentum J_{ns} satisfy a simple phase speed relation (Held 1985): $A_{ns} = c_{ns}J_{ns}$. The phase speed calculated from this relation is hereafter called the theoretical phase speed. It can be written as the sum of an intrinsic phase speed $\hat{c}_{ns}$ plus a Doppler mean speed U_{ns},

$$c_{ns} = \hat{c}_{ns} + U_{ns}, \qquad \hat{c}_{ns} = \frac{\int (E_{ns})\ dS_M}{\int (J_{ns})\ dS_M},$$
$$U_{ns} = \frac{\int \left(\frac{u_0}{\cos\phi}J_{ns}\right) dS_M}{\int (J_{ns})\ dS_M}, \quad (16)$$

where $\int dS_M$ represents an integral over the meridional plane. Notice that the sign of the intrinsic phase speed is controlled by the pseudomomentum only, since the energy is always positive. The Doppler mean speed can be interpreted as a space average of the background wind u_0 weighted by pseudomomentum. A similar decomposition holds for the theoretical frequency ω_{ns} given by the intrinsic frequency $\hat{\omega}_{ns} = s\hat{c}_{ns}/a$ plus a Doppler shift sU_{ns}/a.

If $\boldsymbol{\psi}'^{\mathrm{T}} = (u', v', p', \sigma', q')$ is taken as wave vector, the bilinear forms or metric fields associated with pseudomomentum and pseudoenergy are, respectively,

$$\mathbf{G}_J = \frac{\cos\phi}{2}\begin{pmatrix} 0 & 0 & 0 & 1 & 0 \\ 0 & 0 & 0 & 0 & 0 \\ 0 & 0 & 0 & 0 & 0 \\ 1 & 0 & 0 & 0 & 0 \\ 0 & 0 & 0 & 0 & -\dfrac{\sigma_0^2}{\gamma_0} \end{pmatrix},$$

$$\mathbf{G}_A = \frac{1}{2}\begin{pmatrix} \sigma_0 & 0 & 0 & u_0 & 0 \\ 0 & \sigma_0 & 0 & 0 & 0 \\ 0 & 0 & \lambda p_0^{-k} & 0 & 0 \\ u_0 & 0 & 0 & 0 & 0 \\ 0 & 0 & 0 & 0 & -\dfrac{u_0\sigma_0^2}{\gamma_0} \end{pmatrix}, \quad (17)$$

defined in such a way that the wave activities (14) and (15) can be written as $J = \boldsymbol{\psi}'^{\mathrm{T}}G_J\boldsymbol{\psi}'$ and $A = \boldsymbol{\psi}'^{\mathrm{T}}G_A\boldsymbol{\psi}'$.

b. Construction of the basic state, PCs, and ENMs

In this work, the time- and zonal-average state is used as basic state in the construction of the bilinear forms (17), even though this choice will not necessarily satisfy Eqs. (12) and (13). We verify, however, that the mean winter state of NCEP data approximately obeys these balance equations in most of the upper troposphere and lower stratosphere.

The 850-hPa isobar is taken as the lower boundary of the analysis region. Data below this surface are masked and only the wave activity above it is accounted for in the construction of ENMs. The assumption behind this masking procedure is related to stochastic modeling

in that the neglected wave activity associated with the boundary layer and lower troposphere is supposed to be felt by the upper regions as a random (in time) source.

The meridional gradient of the basic potential vorticity defines the (linear) dynamic stability field γ_0. At large scales, the pseudomomentum of the most relevant ENMs comes primarily from the enstrophy-like component, the second term in Eq. (14). The coefficient of this term (inverse of γ_0) can be thought of as a measure of the local rigidity against PV oscillations. We have observed that regions of large γ_0 coincide with the regions of highest wave activity and the field γ_0 can thus be used as an indicator of preferred domains of wave activity in the upper troposphere and lower stratosphere.

Pseudomomentum has fewer components than does pseudoenergy, which makes it less susceptible to noise and cancellations between components. At large scales, the enstrophy term dominates and pseudomomentum becomes sign definite, as is expected in the quasigeostrophic limit. These properties suggest the pseudomomentum metric as the most convenient for ENM construction, so this is the one used in this study.

To build ENMs we use the time-covariance operator as described in section 2, since the number of available time steps in our data is less than the number of spatial data points. First, anomalies are decomposed as a sum of Fourier modes in the zonal direction,

$$\boldsymbol{\psi}'(t;\,\lambda,\,\phi,\,\theta) = \sum_s \left[\psi_s'^{(1)}(t;\,\phi,\,\theta)\,\cos s\lambda + \psi_s'^{(2)}(t;\,\phi,\,\theta)\,\sin s\lambda\right] \quad (18)$$

and ENMs are generated for each zonal wavenumber s. By construction, the wavenumber-s PCs are orthonormal and satisfy eigenvalue problem (6) with the time-covariance operator given by

$$\tau_s(t,\,t') = \int \frac{\cos\phi}{2} \times \sum_{i=1,2}\left[\sigma_s'^{(i)}(t)u_s'^{(i)}(t') + \sigma_s'^{(i)}(t')u_s'^{(i)}(t) - \frac{\sigma_0^2}{\gamma_0}q_s'^{(i)}(t)q_s'^{(i)}(t')\right] dS_M, \quad (19)$$

where $\int dS_M$ indicates integration over the meridional plane. Given a PC a_{ns}, the algorithm generates a pair of meridional cross sections $[\varphi_{ns}^{(1)},\,\varphi_{ns}^{(2)}]$ for each field, corresponding to the mode's cosine and sine components:

$$\boldsymbol{\psi}'(t;\,\lambda,\,\phi,\,\theta) = \sum_{n,s}\left[\varphi_{ns}^{(1)}(\phi,\,\theta)\,\cos s\lambda + \varphi_{ns}^{(2)}(\phi,\,\theta)\,\sin s\lambda\right]a_{ns}(t), \quad (20)$$

where

$$\varphi_{ns}^{(l)}(\phi,\,\theta) = \overline{\psi_s'^{(l)}(t;\,\phi,\,\theta)a_{ns}(t)}, \qquad l = 1,\,2. \quad (21)$$

c. Calculation of theoretical and observed phase speeds

The theoretical phase speed of a mode is computed from the ratio of its pseudoenergy to its pseudomomentum, which involves the basic state and the ENM spatial structure only. On the other hand, the observed phase speed of a propagating mode is proportional to the mean frequency derived from a pair of time series, as in a complex PC.

The eigenvectors generated by the snapshot method are real-time series, which, in EOF analysis, are interpreted as amplitudes of standing modes. If a propagating mode is present, there should be a pair of eigenvectors, with degenerate eigenvalues, corresponding to the real and imaginary parts (or the sine and cosine Fourier components) of a complex PC, as exemplified by this zonal-wind decomposition:

$$\begin{aligned} u' &= \sum_{n,s}\Re[u_{ns}(\phi,\,\theta)e^{is\lambda}a_{ns}(t)] \\ &= \sum_{n,s}\{\Re[u_{ns}(\phi,\,\theta)]\,\cos s\lambda - \Im[e_{ns}(\phi,\,\theta)]\,\sin s\lambda\} \\ &\quad\times \Re[a_{ns}(t)] \\ &\quad - \sum_{n,s}\{\Im[u_{ns}(\phi,\,\theta)]\,\cos s\lambda + \Re[u_{ns}(\phi,\,\theta)]\,\sin s\lambda\} \\ &\quad\times \Im[a_{ns}(t)]. \end{aligned} \quad (22)$$

Here $\Re[\cdots]$ and $\Im[\cdots]$ indicate real and imaginary parts. Given a zonal wavenumber s, if the mth and nth modes obey $\varphi_{ms}^{(1)} = \pm\varphi_{ns}^{(2)}$ and $\varphi_{ms}^{(2)} = \mp\varphi_{ns}^{(1)}$, then they form a propagating pair and the PCs a_{ms}, a_{ns} provide the real and imaginary parts of a complex PC $A_{ns} = a_{ms} + ia_{ns}$. The average frequency (hereafter called observed frequency) is thus calculated according to the recipe $\overline{\omega} = \overline{A^* i\dot{A}}/\overline{|A|^2}$. This was the approach used to find the wavenumber-5 quasi mode (see section 5) and construct the associated power spectrum.

The above method requires visual recognition of similar spatial pattern, which may sometimes be straightforward but in most cases is impractical. The separation of nondegenerate eigenvalues is also a statistical issue (see, e.g., North 1984). There is a second approach, which assumes that existing propagating pairs tend to be sorted as near neighbors when the snapshot method organizes PCs in decreasing order of eigenvalues. We therefore suppose that the modes $[\varphi_{n,s},\,\varphi_{n+1,s}]$ form a pair, that the associated time series constitute a complex PC, $A_{n,s} = a_{n,s} + ia_{n+1,s}$ from which we can construct the mode's power spectrum, mean frequency, and phase speed.

One could also compute higher moments of the frequency spectrum, such as $\overline{\omega^2} = \overline{|\dot{A}|^2}/\overline{|A|^2}$, but previous studies (Brunet and Vautard 1996) indicate that the value derived from the first moment $\overline{\omega}$ is the one that should be compared with the theoretical frequency (see section 3a).

d. Diagnostic output

The algorithm takes as input a dataset of wind, pressure, specific volume, and potential vorticity in isentropic coordinates, and produces the following output: (i) the time-zonal mean, which is used as basic state [a balance test based on equations (12) and (13) is also provided]; (ii) a plot of the dynamic stability field γ_0 and regions of high wave activity; (iii) a complete decomposition of transients in terms of PCs and ENMs, for chosen values of the zonal wavenumber; (iv) detailed spectra of pseudomomentum and pseudoenergy; (v) observed and theoretical phase speeds and periods, calculated from PCs and from ratios of wave activity. A reconstruction routine is also available for comparison of data with any truncated series of ENMs.

4. Dataset

A sequence of four consecutive winters is taken from NCEP reanalyses, December–January–February of 1988–91, with time series sampled at 6-h intervals. Data are then interpolated onto isentropic coordinates, using the method described in Edouard et al. (1997). The resulting dataset consists of five fields: horizontal wind (u, v), pressure p, specific volume α, and potential vorticity q. The four winters are then merged as one continuous time series, discontinuities between consecutive years being disregarded due to their small statistical significance. The vertical resolution is nonuniform, consisting of 16 isentropic levels chosen to favor and better resolve upper-tropospheric and lower-stratospheric regions. The horizontal grid is global and has 32 latitude circles and 22 meridians. In this diagnostic study we only consider zonal wavenumbers up to $s = 9$. This dataset allows an analysis of large synoptic scales and larger.

5. Diagnostic results

a. Validation tests

The algorithm was validated with exact solutions of the linearized primitive equations. Two kinds of exact solutions were used: superpositions of nondivergent planetary waves propagating on isothermal basic states, with and without a simple (solid rotation) background wind; and linear combinations of irrotational gravity waves on a nonrotating sphere. The vertical dependence of these solutions is separable and the horizontal structure satisfies the well-known Laplace tidal equations studied by Longuet-Higgins (1968). The algorithm was able to separate the propagating modes cleanly and produce the correct values of wave activity. Moreover, the theoretical and observed phase speeds produced by the algorithm matched very accurately the expected values of the analytical solutions.

b. Basic-state characteristics

Figure 1 shows the four-winter zonal climatology of zonal wind, pressure, specific volume, and potential vorticity, from which the basic state is constructed. Similar climatological fields were found by Edouard et al. (1997) using a 10-winter period form European Centre for Medium-Range Weather Forecasts (ECMWF) analyses.

The northern jet stream of the basic zonal wind (Fig. 1a) has a maximum of $\sim$42 m s^{-1} at $\phi = 30°$N, $\theta = 345$ K, whereas the southern jet peaks at $\sim$28 m s^{-1} near $\phi = 50°$S, $\theta = 345$ K. The basic meridional wind speeds are at least one order of magnitude smaller than the jet maximum, which ultimately justifies the choice $v_0 \approx 0$ in the bilinear forms of wave activities. The thermal wind balance (12) is verified within 10%.

At low latitudes, the basic pressure field (Fig. 1b) exhibits a nearly uniform, bell-shaped plateau that contains part of the boundary layer as well as some closed contours of 1000 hPa—the latter are not physically meaningful, as they come from interpolation of tropical unstable domains into θ coordinates. Major vertical pressure gradients occur below the 330-K level, between the 450- and 950-hPa isobars. The 850-hPa isobar, indicated by a dot–dash line, separates the lower troposphere from the upper domain; wave activities below this surface are masked.

Basic pressure and specific volume are supposed to be in hydrostatic balance, and the climatology verifies this property except in the case of some regions near the ground and around the tropopause. Near-ground regions are eventually masked and have therefore no direct effect on the ENM calculation. The hydrostatic imbalance near the tropopause is explained by the large variability of fields in this region, as indicated by the expansion

$$\frac{\partial p}{\partial \theta} = -\frac{g}{\alpha} \Rightarrow \frac{\partial [p]}{\partial \theta} = -\frac{g}{[\alpha]}\left\{1 + O\left(\frac{[\alpha'^2]}{[\alpha]^2}\right)\right\}, \qquad \alpha' = \alpha - [\alpha], \tag{23}$$

where $\alpha = 1/\sigma =$ specific volume and $[\cdots]$ means time-zonal average. Finite-difference errors in the calculation of the vertical pressure gradient turn out to be small compared with the variability effect. This problem inspired some modified diagnostic experiments, with the basic specific volume constructed so as to obey the hydrostatic constraint. However, for the large scales we are interested in, this modification was shown to have a minor impact on the diagnosis.

The mean PV field (Fig. 1d) is dictated in the vertical by the density profile and in the meridional direction by the planetary vorticity. The linear stability field γ_0 associated with the basic state is computed from the meridional PV gradient, according to Eq. (14). A perhaps more intuitive version of the stability field γ_{qg}, weighted by the basic density, is defined according to

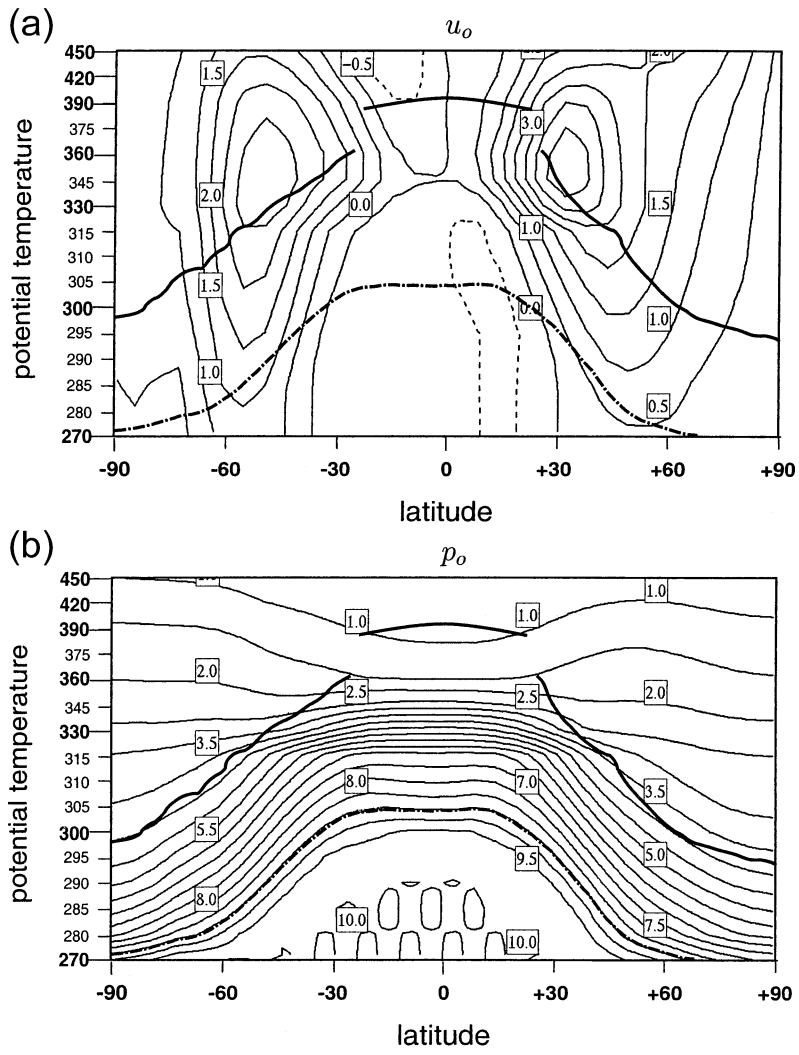

FIG. 1. Meridional cross sections showing the time–zonal average fields, constructed out of four consecutive winters from NCEP reanalyses: (a) zonal wind u_0 (in units of 10 m s^{-1}); (b) pressure p_0 (in units of 100 hPa); (c) specific volume α_0 (in units of 10^{-2} K m^2 kg^{-1}); (d) potential vorticity q_0 (in units of 10^{-5} K m^2 kg^{-1} s^{-1}). The meridional gradient of the mean potential vorticity, normalized by the basic specific volume, defines the stability field $\gamma_{qg} = (\partial q_0/\partial\phi)/a\alpha_0 \cos\phi$ shown in (e) (in units of 10^{-11} m^{-1} s^{-1}). (f) The time–zonal mean of the (quasigeostrophic) enstrophy of transients, $\Sigma_{s=1}^{9}\ \sigma_0\overline{Q_s'^2}$ (in units of 3.9×10^{-7} kg m^{-2} K^{-1} s^{-2}). The mean tropopause (marked by a thick solid line) is defined by $q_0 = 2 \times 10^{-6}$ K m^2 kg^{-1} s^{-1} at latitudes $|\phi| > 25°$ and by $\theta \sim 390$ K at $|\phi| < 25°$, according to Hoskins and Karoly (1981). The separation between lower and upper troposphere is indicated by a thick dot–dash line.

the quasigeostrophic version of enstrophy, as sketched below:

$$\int \left(\frac{\sigma_0^2 \cos\phi}{2\gamma_0} q'^2\right) dV \approx \int \left(\frac{1}{2\gamma_{qg}} Q'^2\right) \sigma_0 dV,$$

$$Q' = \sigma_0 q', \qquad \gamma_{qg} = \sigma_0 \frac{\partial q_0}{\partial(a \sin\phi)}, \tag{24}$$

where $\int \sigma_0\, dV$ indicates a sum over mass elements and Q' is a normalized PV disturbance defined to provide the convenient quasigeostrophic limit (Andrews et al. 1987). The role of the mean PV-gradient as an indicator of instability of the basic state is well known, but it might also be useful to think of the stability field as the inverse of the background rigidity against variations of PV. As shown in Fig. 1e, γ_{qg} exhibits a pair of ridges with maxima at midlatitudes just below the tropopause, where large amplitudes of pseudomomentum and intense wave activity are indeed observed (see also Fig. 1f).

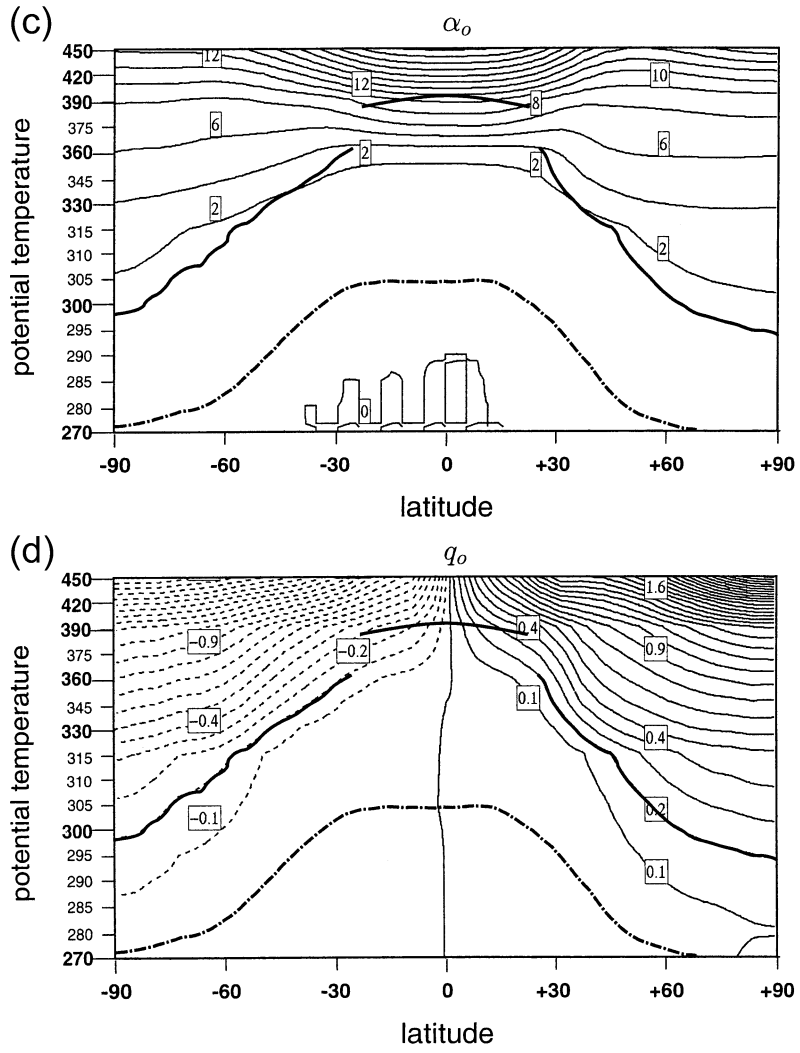

FIG. 1. (*Continued*)

c. Ordering modes: The ENM number n

After looking at results and trying different options, we decided to sort the ENMs according to increasing pseudomomentum and to label them with the mode number n, such that $n = 1$ has the smallest (most negative) pseudomomentum, $n = 2$ has the next smallest value, and so on. Although the index n has no obvious geometrical meaning, it provides a convenient ordering: on the one hand, ENMs are sorted according to their ''activity'' (measured by the absolute value of pseudomomentum) and, on the other hand, modes dictated by vorticity (with negative pseudomomentum, small n) are separated from the branch of divergent modes (with positive pseudomomentum, large n). The transition region, where pseudomomentum approaches zero, often corresponds to small-scale ENMs.

To establish a relation between the index n and scales, we have calculated the mean meridional wavenumber $\langle l \rangle_{ns}$ and the mean vertical wavenumber $\langle m \rangle_{ns}$ of each ENM using the definitions

$$\langle l \rangle_{ns} = \left\{ \frac{\int \left| \frac{\partial}{\partial \phi} v_{ns} \right|^2 dS_M}{\int |v_{ns}|^2 \, dS_M} \right\}^{1/2},$$

$$\langle m \rangle_{ns} = \left\{ \frac{\int \left| \frac{\partial}{\partial \ln\theta} v_{ns} \right|^2 dS_M}{\int |v_{ns}|^2 \, dS_M} \right\}^{1/2}, \qquad (25)$$

where v_{ns} is the meridional wind component of the (ns)th ENM and $\int dS_M$ indicates an integral over the meridional plane as before. Figure 2 shows results obtained with

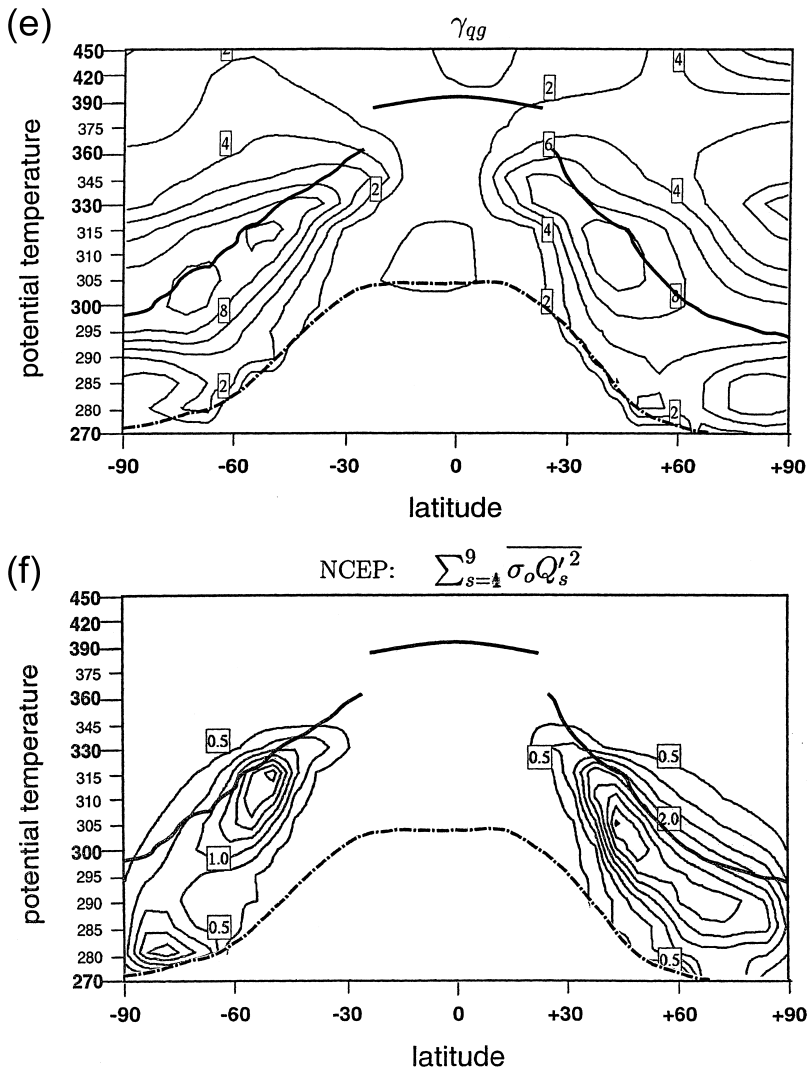

FIG. 1. (*Continued*)

wavenumber $s = 5$, an interpretation being given in the next section for various ranges of the index n.

d. Wave activity spectrum

The wave activity spectra found in this study are relatively smooth and follow a pattern that is depicted schematically in Fig. 3 and described below.

- In range I (small n), the pseudomomentum of large-scale modes is dominated by the PV term, density oscillations are relatively small. Both pseudoenergy and pseudomomentum are negative, so the linear theory predicts that modes propagate eastward according to the phase speed relation $A_{ns} = c_{ns}J_{ns}$.
- Transition from range I to II is characterized by a balance between the energy and Doppler terms, when the pseudoenergy basically vanishes while the pseudomomentum, still dictated by PV oscillations, does not. Using the relation $A_{ns} = c_{ns}J_{ns}$ from linear theory, these should behave as stationary modes.
- Range II, with intermediate values of n, has positive pseudoenergy (energy larger than Doppler term) and negative pseudomomentum (density oscillations become more important, but the PV term still dominates), thus modes propagate westward.
- The transition from range II to III is marked by the null eigenvector whose amplitude is virtually zero everywhere.
- In range III both the pseudoenergy and the pseudomomentum are positive. Even though modes propagate eastward as in range I, now the momentum term exceeds the PV component.
- The mean wavenumbers $\langle l \rangle_{ns}$ and $\langle m \rangle_{ns}$ increase with n in ranges I and II, reach a maximum between ranges

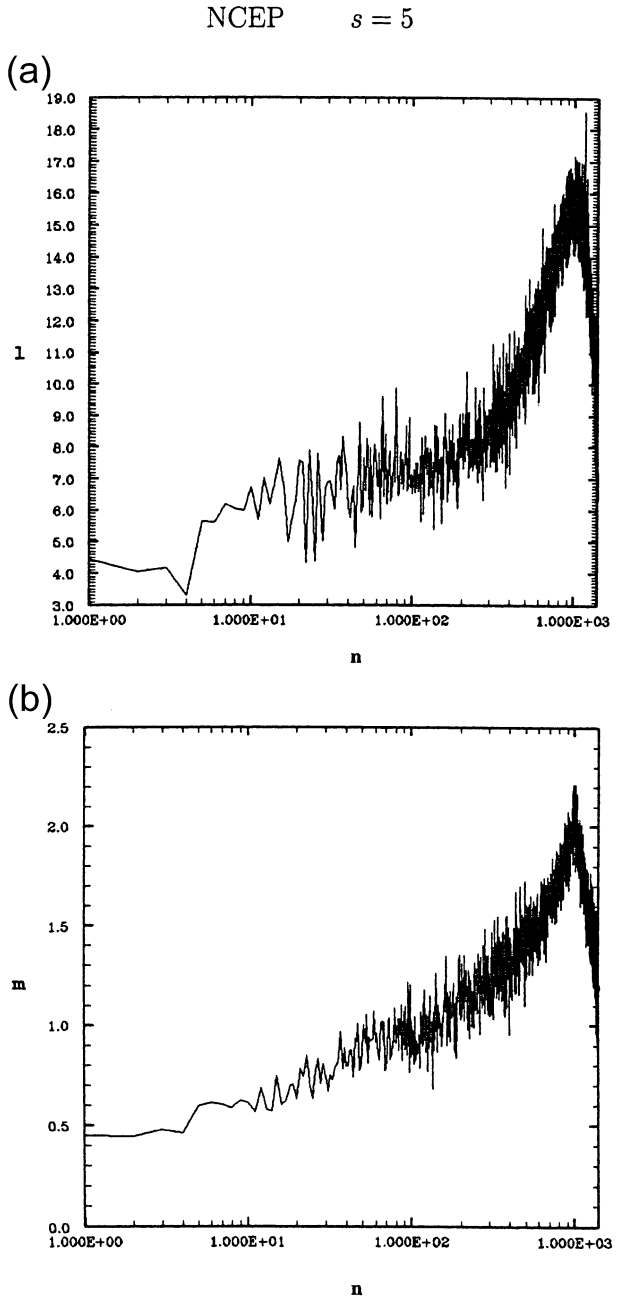

FIG. 2. Relation between the ENM number n and (a) the mean meridional wavenumber $\langle l \rangle$ and (b) the mean vertical wavenumber $\langle m \rangle$, for modes with zonal wavenumber $s = 5$. The maximum at large values of n corresponds to vanishing pseudomomentum.

II and III, and decrease with n in range III. This behavior confirms that the ENM number n can be used as a measure of spatial scales, but the relation between n and wavenumbers depends on the range.

The transitions described above may occur at different values of n for different zonal wavenumbers, but the picture is basically the same for every s. To illustrate these properties, the absolute values of pseudoenergy and pseudomomentum of ENMs with zonal wavenumbers $s = 1$, 5, and 9 are plotted in Fig. 4. Similar curves are obtained with other wavenumbers.

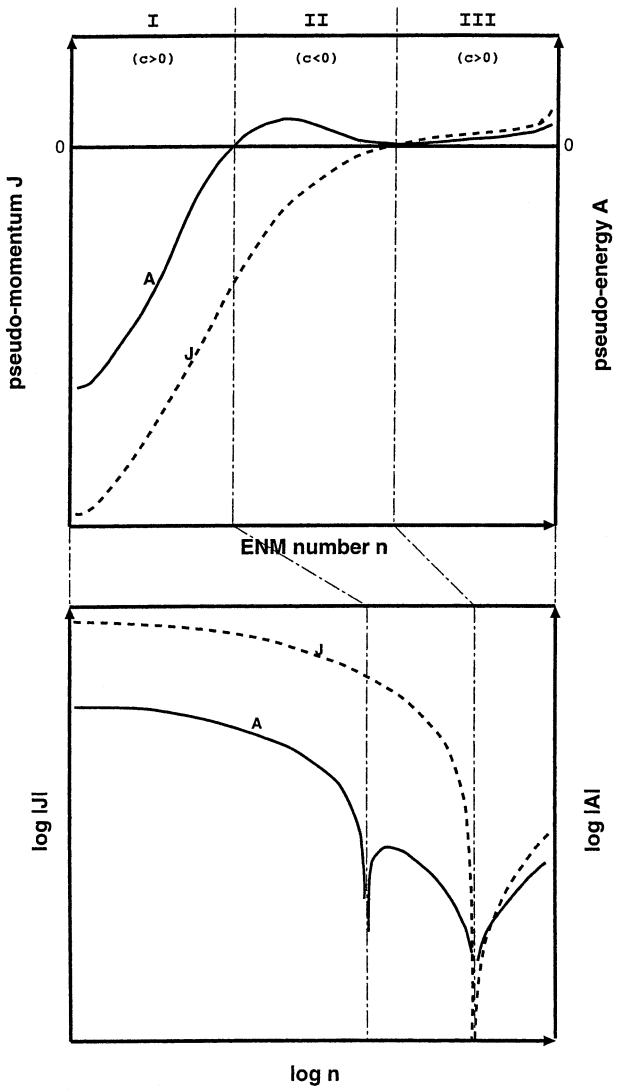

FIG. 3. Qualitative picture of typical spectra of pseudomomentum J and pseudoenergy A for a fixed zonal wavenumber.

The partition of pseudoenergy is plotted in Fig. 5. Concerning large-scale (small n) modes, where large amplitudes reside, two characteristics stand out.

- Pseudoenergy is dominated by the vorticity term, followed by the kinetic energy, potential energy and a small, noisy contribution from the Doppler momentum term. This partition is compatible with a picture of vortical modes.
- ENMs with small zonal wavenumbers ($s < 3$) exhibit an approximate equipartition of kinetic and potential energy. As s increases, the kinetic energy gradually exceeds the potential term, in agreement with the quasi-

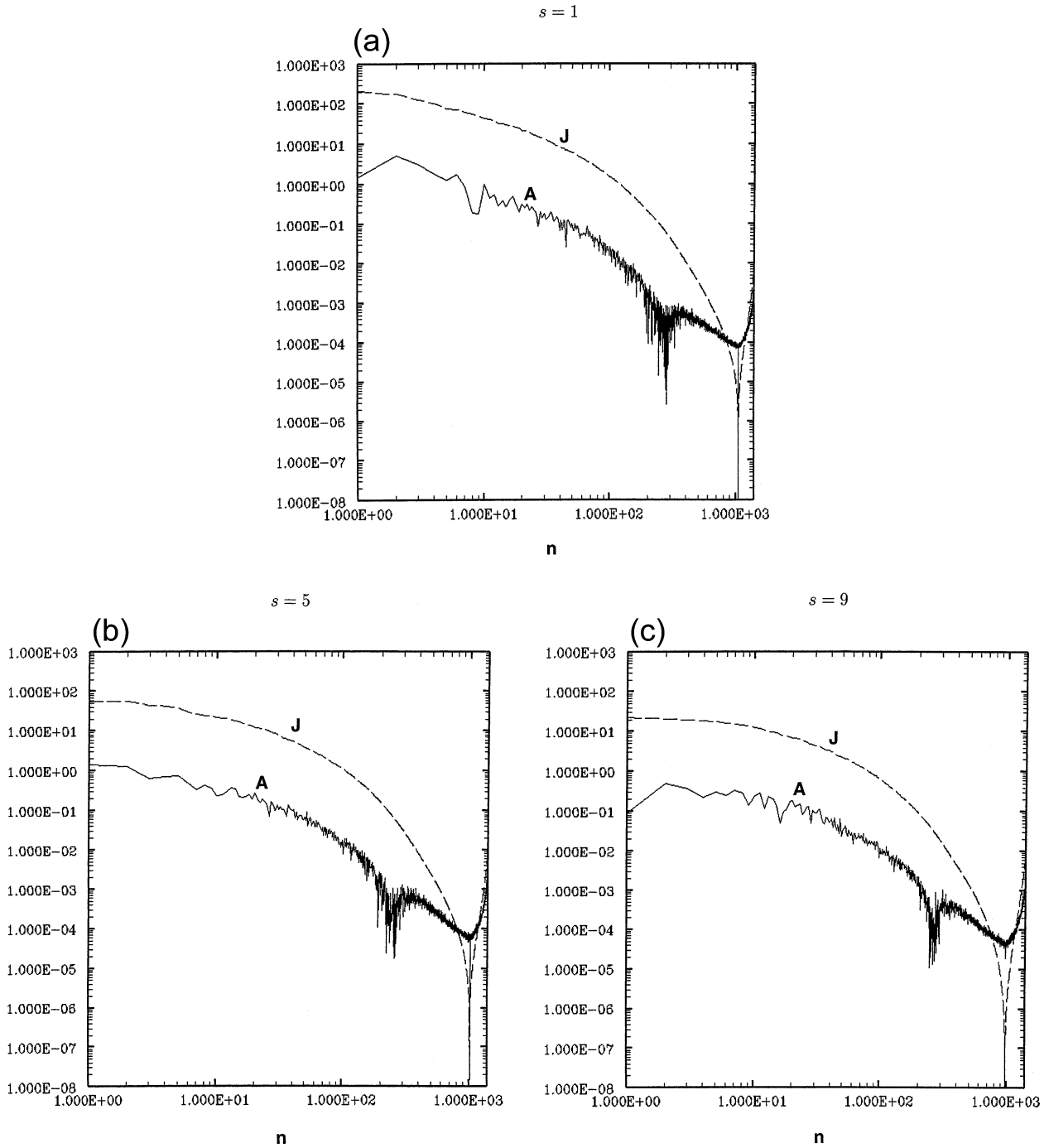

FIG. 4. Spectra of absolute values of the pseudomomentum (J, in units of 2.70×10^3 kg m^{-1} s^{-1}) and the pseudoenergy (A, in units of 1.25×10^6 J m^{-2}) of ENMs with zonal wavenumbers (a) $s = 1$, (b) $s = 5$, and (c) $s = 9$. Note that J changes sign at the cusp and becomes positive for high values of n.

geostrophic theory (Gill 1982) in which planetary waves obey the relation

$$\frac{\text{kinetic energy}}{\text{potential energy}} = k_h^2 a_R^2, \tag{26}$$

where k_h represents the horizontal wavenumber, and a_R is the Rossby radius.

Because of these characteristics, small n ENMs are hereafter called large planetary ENMs.

On the extreme right of the spectrum, energy levels

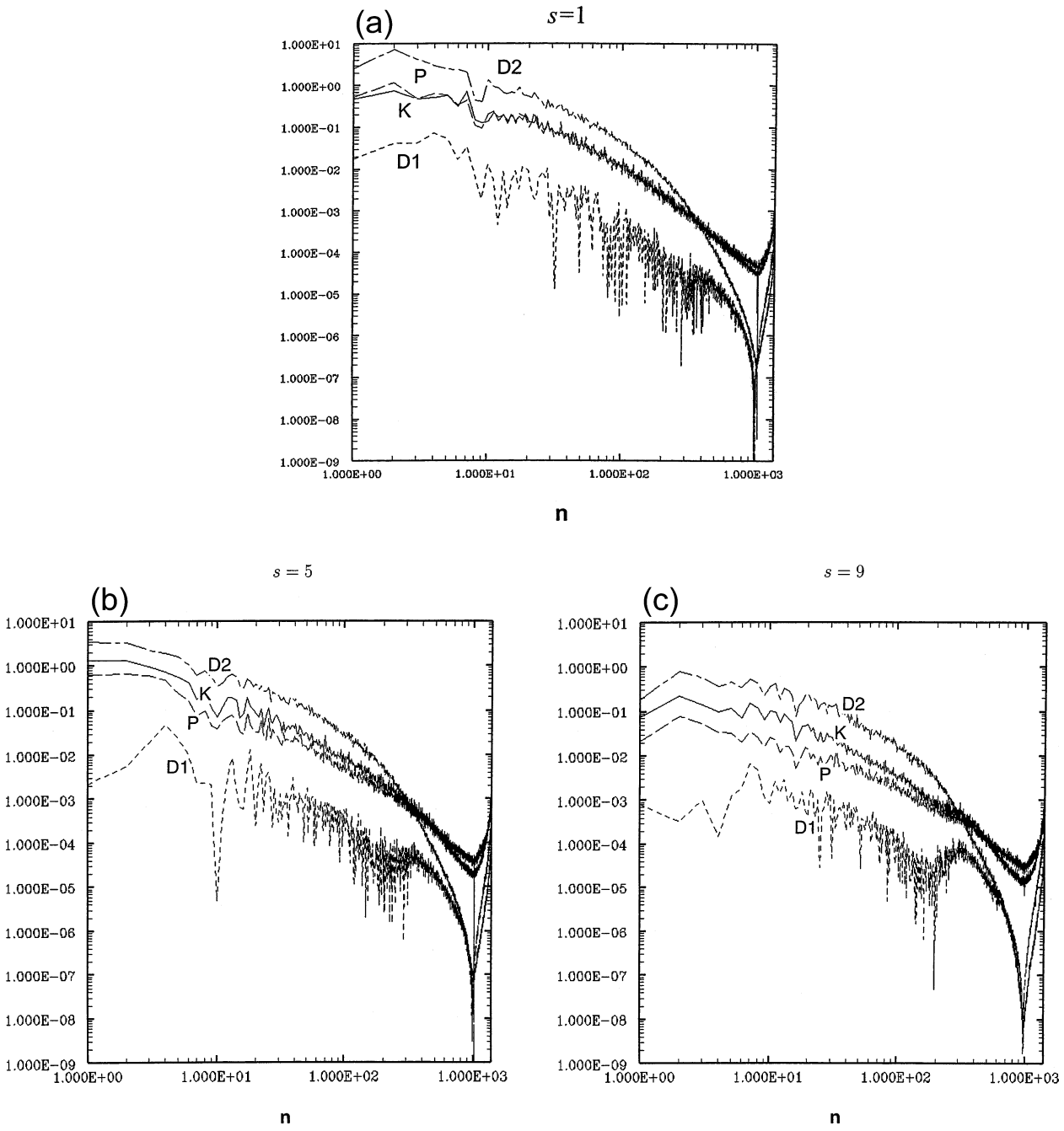

FIG. 5. Partition of pseudoenergy into four components: kinetic energy (K), potential energy (P), Doppler momentum ($D1$), and Doppler PV term ($D2$) according to Eq. (15), for wavenumbers (a) $s = 1$, (b) $s = 5$, and (c) $s = 9$. (All in units of 1.25×10^6 J m^{-2}.)

are two to three orders of magnitude smaller than those of planetary modes. Still the kinetic and potential energies seem to converge towards equipartition, for all zonal wavenumbers. Both Doppler terms (momentum and PV terms) make comparable contributions. These modes are therefore intrinsically different from large planetary modes, even though they propagate in the same direction—both branches have positive (theoretical) phase speeds.

In the intermediate range of the spectrum, modes propagate in both directions. Their pseudoenergy is largely dominated by kinetic and potential contributions, with negligible Doppler shifts. These properties resemble those of gravity or Rossby–gravity modes, but their small amplitudes and scales may lie beyond the limited resolution of the data.

The partition of pseudomomentum is shown in Fig. 6. The PV term largely dominates in large planetary

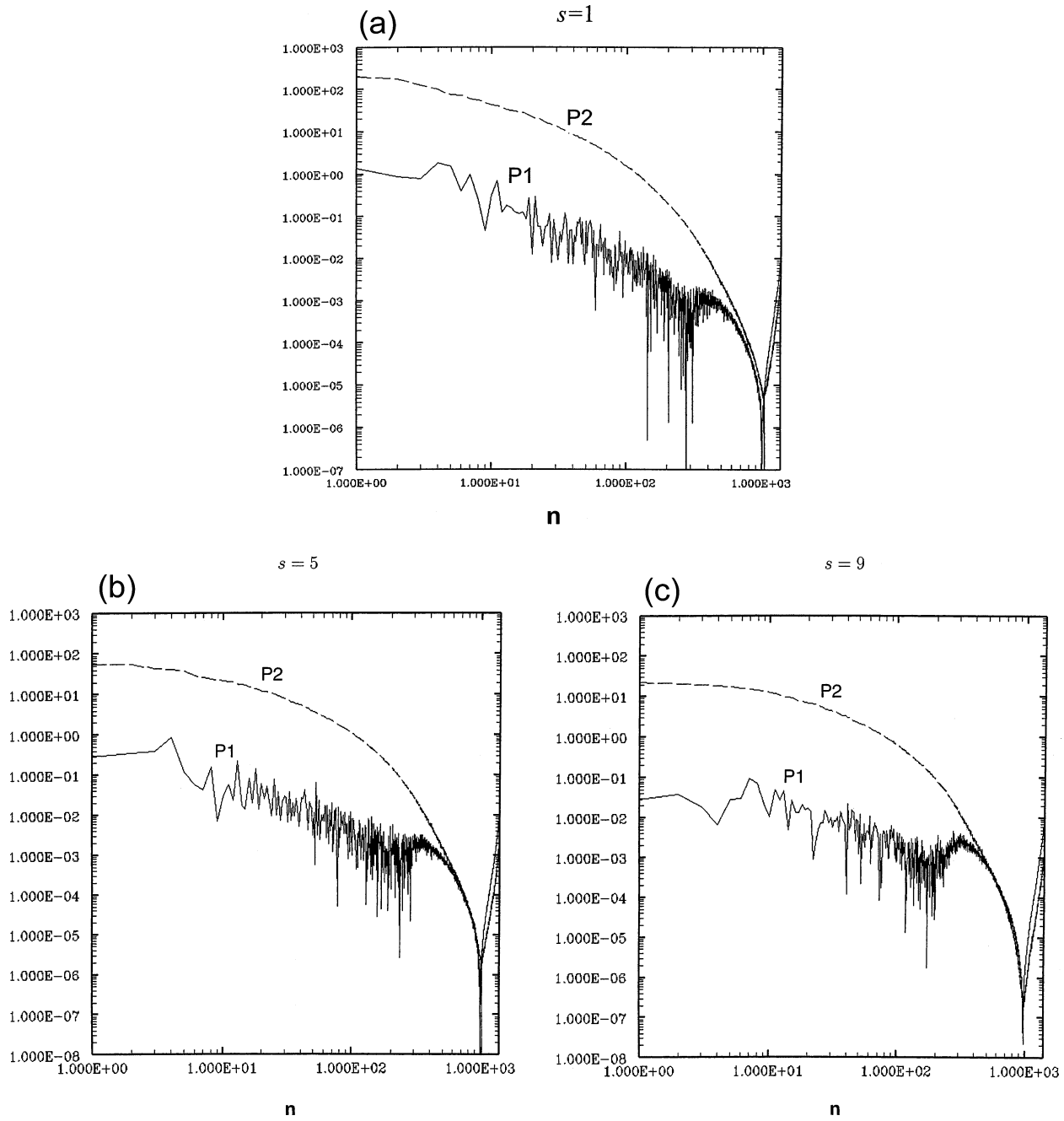

FIG. 6. Partition of pseudomomentum into two components: momentum ($P1$) and PV term ($P2$), as in Eq. (14), for wavenumbers (a) $s = 1$, (b) $s = 5$, and (c) $s = 9$ (in units of 2.70×10^3 kg m^{-1} s^{-1}).

modes, up until the intermediate range of the spectrum where the momentum contributions become equally important. Curves of the PV component are smooth and change sign only once, near the zero eigenvector. The momentum spectrum, on the other hand, is noisy and often changes sign in the small n range, once again indicating that density variations give just a noisy contribution to large-scale modes, but it becomes smooth at large values of n and has mostly the same sign as the PV term.

Previous studies, such as the work by Boer and Shepherd (1983), have used Fourier or spherical harmonics to decompose the data at every vertical level and calculate the wave energy spectrum in terms of a two-dimensional scale index k. Comparisons with wave activity spectra in terms of the ENM index n are not

TABLE 1. Exponents b and d obtained from power-law fits of the kinetic energy $E_{kin} \sim n^{-b}$ and potential energy $E_{pot} \sim n^{-d}$ in two different subranges of the ENM index n for wavenumbers $s = 1$, 5, and 9.

		$s = 1$	$s = 5$	$s = 9$
Small n subrange	b	0.9	1.6	1.7
	d	0.9	1.4	1.4
Intermediate n subrange	b	2.8	3.5	3.6
	d	2.5	2.5	2.3

straightforward because our ENM analysis is three-dimensional and the relation between n and the usual space-scale indices is not simple. At small scales, Boer and Shepherd have found an approximate equipartition among the zonal and meridional components of kinetic energy and available potential energy, which gives total kinetic energy E_{kin} twice as large as available potential energy E_{pot}. We also observe this tendency at large values of the wavenumber s (see detailed pseudoenergy spectrum at $s = 5$ and 9 for instance) but not at small values such as $s = 1$ where $E_{kin}/E_{pot} \sim 1$. The transition from the regime $E_{kin}/E_{pot} \sim 1$ at small values of s to the regime $E_{kin}/E_{pot} \sim 2 - 3$ at larger s is gradual [see Longuet-Higgins (1968) for a similar behavior of shallow water modes on the sphere].

The energy spectra generated by the ENM analysis exhibit subranges that can be approximately described by power laws such as $E_{kin}(n) \propto n^{-b}$ and $E_{pot}(n) \propto n^{-d}$. In spite of the difficulties in translating the index n in terms of spatial scales this power-law behavior suggests an interpretation in terms of inertial ranges, as is usual in turbulence theories. Table 1 provides the calculated values of slopes of kinetic and potential energy in two subranges for $s = 1$, 5, and 9. Pseudomomentum curves (Fig. 6), on the other hand, seem to display exponential rather than power-law behavior. In the absence of further theoretical predictions on turbulent energy spectrum in normal mode space at the larger-than-synoptic scales, the explanation of these diagnostic results is left as an open question.

Finally, let us consider the transition range, where both wave activities tend to vanish. According to linear theory, such modes are unstable, and one might think of looking for unstable ENMs in this range. However, in some cases the wave activity of unstable modes is supposed to have important surface contributions, which we have not taken into account. The algorithm, in its present form, cannot clearly diagnose these kinds of unstable modes.

e. ENM's characteristics

For each pair of parameters (n, s), the algorithm generates 10 meridional cross sections, which are the sine and cosine components of five fields: the mode's zonal wind, meridional wind, pressure, specific volume, and PV.

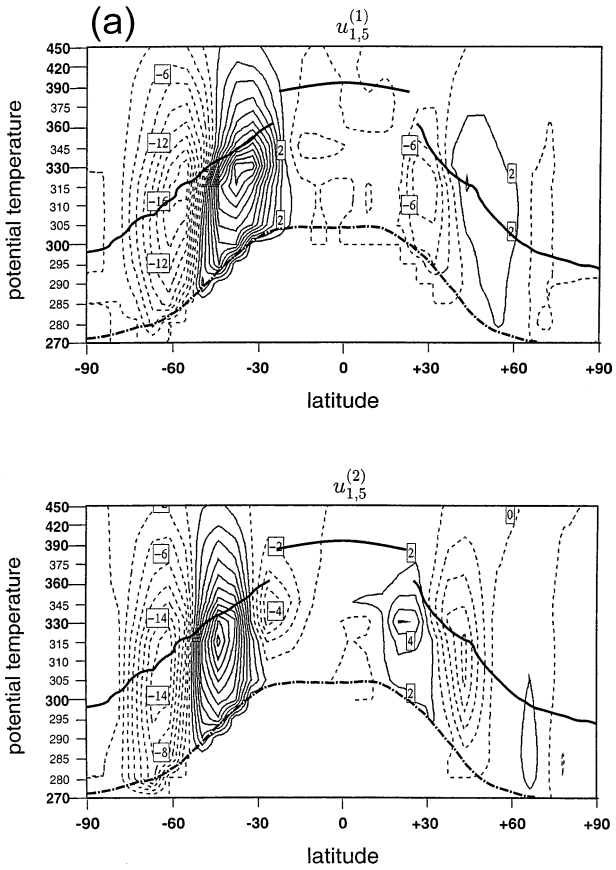

FIG. 7. Meridional cross sections showing the meridional profile of the leading wavenumber-5 ENM, separated into the cosine (1) and sine (2) components of (a) zonal wind, (b) meridional wind, (c) pressure, (d) specific volume, and (e) PV. Amplitudes are normalized by the basic-state fields according to formula (15) to indicate local contributions to the pseudoenergy: winds are multiplied by $\sigma_0^{1/2} = \alpha_0^{-1/2}$, pressure by $(\lambda p_0^{-k})^{1/2}$, and PV by $\sigma_0 |u_0/\gamma_0|^{1/2}$. Specific volume is simply normalized by the basic-state α_0. The thick solid line indicates the mean tropopause and the dot–dash line separation indicates the separation between lower and upper troposphere.

Let us first describe the general features of large-scale ENMs (figures are not shown). Their meridional dependence is observed to vary with the zonal wavenumber: for small values of s (basically $s \leq 2$), the amplitude of the most energetic modes is centered at high latitudes, mainly near the North Pole; planetary modes with intermediate wavenumbers ($3 \leq s \leq 5$) have large amplitudes at midlatitudes; and for $s \geq 6$, wave activity migrates to mid- and low latitudes. Concerning vertical structures, wind components (u', v') have an approximate equivalent barotropic pattern, although most of the kinetic energy is concentrated below the tropopause; on the other hand, pressure components p' show multipolar structures, organized around the tropopause, such that potential energy is found both in the troposphere and the stratosphere. The meridional structures of specific volume α' and PV components q' are compatible with

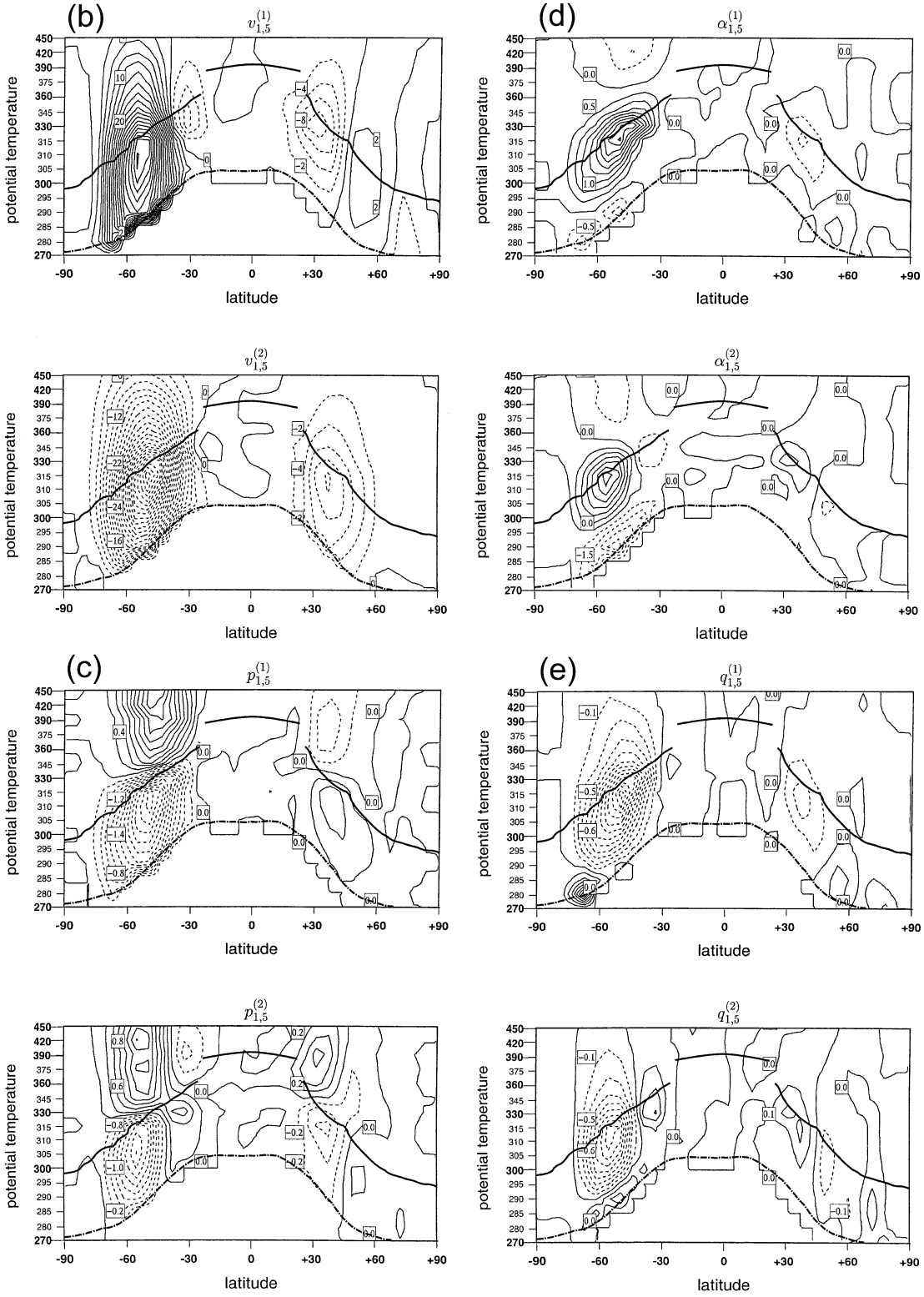

FIG. 7. (*Continued*)

pressure and wind patterns, in the sense that they follow the relations predicted by the linearized theory.

As an example of the above properties, the first and most energetic wavenumber-5 mode $\varphi_{1,5}$ is shown in Fig. 7. Its wave activity concentrates in the Southern (summer) Hemisphere, in agreement with previous studies (Lin and Chan 1989), even though relatively small amplitudes can also be seen in the Northern Hemisphere—such connection between hemispheres has no dynamical meaning and could be eliminated by a rotation in ENM space.

On the small-scale range of the spectrum, ENMs show patterns of wave activity at all latitudes. Figure 8 gives an example of simultaneous equatorial and midlatitude activity. However, some of these modes have meridional and vertical scales that are not well resolved by the grid used here. They also tend to have small amplitudes, making it difficult to separate modes from one another and from noise. We were unable to identify Kelvin modes, probably due to coarse vertical resolution of the data. Due to limited resolution, a more satisfactory diagnosis of small-scale modes has to be postponed.

f. Empirical quasi modes

We chose to present the ENM $\varphi_{1,5}$ not only to illustrate properties of large-scale modes but because its characteristics are compatible with those of a quasi mode. The excitation and maintenance of quasi modes as a model for upper-tropospheric synoptic-scale waves was originally proposed by Rivest et al. (1992) and Rivest and Farrell (1992). They defined quasi modes as special combinations of singular modes, with a distribution sharply peaked in the phase speed domain.

The dominant ENMs, which have the largest values of wave activity, may not be ordinary unstable modes. As linear theory predicts, unstable modes have zero wave activity (Held 1985). Also, the dipolar structure of the pressure mode $p_{1,5}$ resembles the equivalent quasi-modal pattern found by Rivest et al. (1992). Another indication of quasi-modal behavior comes from a matching of decay times calculated in three independent ways.

- The decay time Λ_{obs} may be defined in terms of the spectral width $\Delta\omega$:

$$\Lambda_{\text{obs}}^{-1} = \Delta\omega = \sqrt{\overline{\omega^2} - \overline{\omega}^2},$$

$$\overline{\omega^m} = \int \omega^m |\tilde{a}_{1,5}|^2 \, d\omega, \tag{27}$$

$|\tilde{a}_{1,5}|^2$ = mode's power spectrum. In this case, we found $\Lambda_{\text{obs}} = 3.2$ days.

- The quasi-mode theory of Rivest et al. predicts a decay rate proportional to the mode intrinsic frequency $\Lambda^{-1} = 0.45|\hat{\omega}|$. Based on phase speed relation (16), we calculated the theoretical decay time Λ_{th} using energy and pseudomomentum:

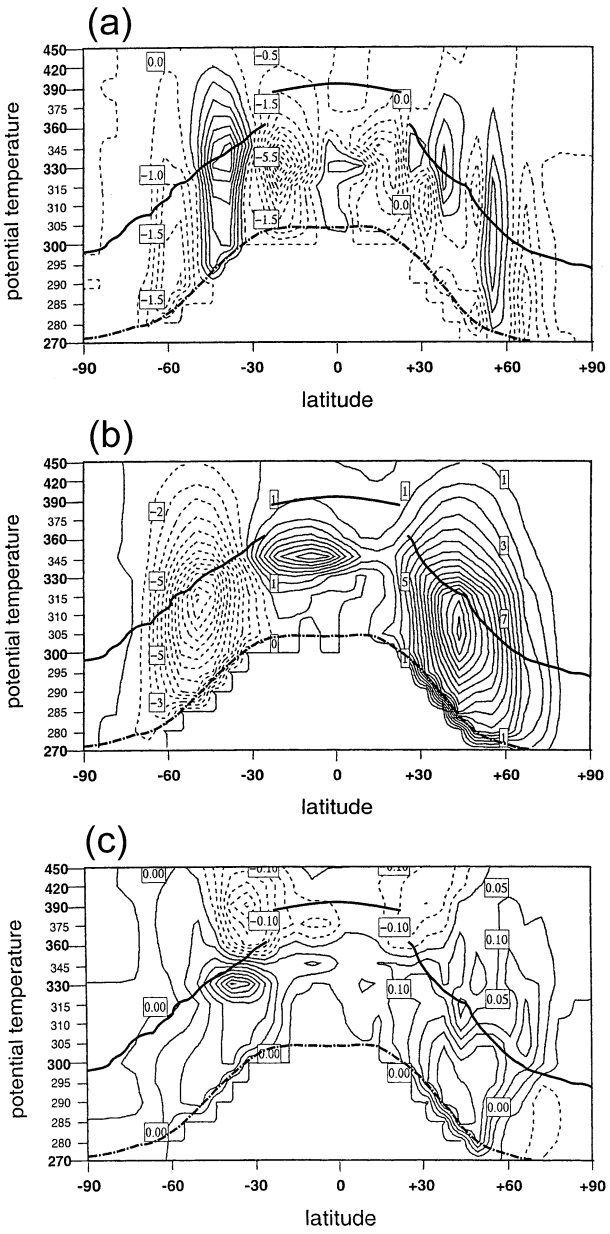

FIG. 8. Cross section of the cosine component of the ENM $n = 4$, $s = 8$, displaying wave activity at low and midlatitudes, simultaneously: (a) zonal wind, (b) meridional wind, and (c) pressure components. Fields are normalized as in Fig. 7.

$$\Lambda_{\text{th}}^{-1} = 0.45 \left| \frac{s}{a} \frac{\int (E_{1,5}) \, dS_M}{\int (J_{1,5}) \, dS_M} \right| \quad \text{with } s = 5 \tag{28}$$

and the result was $\Lambda_{\text{th}} = 2.8$ days.

- The empirical, quasigeostrophic formula of Rivest et al. for the decay rate of quasi modes is

TABLE 2. Observed (T_{obs}, c_{obs}) and theoretical (T_{th}, c_{th}) values of the mean period in days, and phase speed (m s^{-1}), of some leading modes with wavenumbers $s = 1$, 5, and 9.

s	n	T_{obs}	T_{th}	C_{obs}	C_{th}
1	1	100	55	4.6	8.4
1	3	63	44	7.4	10.6
1	5	39	48	11.9	9.7
1	7	94	106	4.9	4.4
1	10	60	58	7.7	8.0
1	15	94	88	4.9	5.3
5	1	6.6	8.0	14.1	11.6
5	3	9.1	12.0	10.2	7.7
5	4	10.4	11.0	8.9	8.4
5	5	15.0	11.0	6.2	8.4
5	7	8.4	13.0	11.1	7.1
5	12	14.0	11.0	6.6	8.4
5	15	9.7	14.0	9.6	6.6
5	17	12.0	12.0	7.7	7.7
9	2	3.4	5.2	15.2	9.9
9	3	6.6	7.0	7.8	7.4
9	7	4.4	5.4	11.7	9.6
9	8	6.4	7.3	8.1	7.1
9	9	7.1	7.6	7.3	6.8
9	15	12.0	9.9	4.3	5.2
9	16	11.0	12.0	4.7	4.3

$$\Lambda_{qm}^{-1} = 0.45\frac{\beta k}{k^2 + l^2}. \quad (29)$$

For $s = 5$, 45° of latitude, a channel width of 3300 km, and the β appropriate to the upper troposphere (see Rivest and Farrell 1992), we get $\Lambda_{qm} = 2.9$ days.

The observed and theoretical phase speeds of the mode $\varphi_{1,5}$, 12–14 m s^{-1}, are also compatible with the quasi-mode estimate $c_{qm} = \overline{U} - \beta/(k^2 + l^2)$ if $\overline{U} \approx 20$ m s^{-1} (note that mean wind speeds of the Southern Hemisphere summer jet vary from 10 to 30 m s^{-1} in the upper-tropospheric channel).

g. Comparison of characteristic periods

Principal components are used to compute (observed) phase speeds and periods as described in section 3, while theoretical values are calculated from ratios of wave activities. In the previous section, the period and phase speed of a wavenumber-5 quasi mode were presented, and Table 2 shows other examples of observed and theoretical values for modes with wavenumbers $s = 1$, 5 and 9.

As concerns the leading, large planetary ENMs (small n range of the spectrum) we observe the following behavior.

- Modes with wavenumbers $s < 3$ have a broad power spectrum dominated by small frequencies. In this case, we have used the nearest-neighbor approach to generate the observed phase speeds and periods shown in Table 2. Periods are comparable to the 3-month period of the winter seasons considered in this work, making calculations more difficult as was previously observed in studies of the shallow water model (Brunet and Vautard 1996).
- At wavenumbers $s \geq 5$, the power spectrum of the leading modes tend to have prominent peaks and we obtained mean frequencies compatible with theoretical values, as shown in Table 2. This approximate matching of periods is interpreted as a success of the description in terms of stochastically forced normal modes (Charron and Brunet 1999).

At larger values of n the comparison of observed and theoretical periods is much less successful, which can be attributed to nonlinearities and the problems of degeneracy, low resolution, and small amplitude since ENMs in this range are characterized by small structures and relatively small values of wave activity.

6. Summary and conclusions

We have presented a diagnostic algorithm, based on the ENM technique, that can be used in the decomposition of atmospheric disturbances and in studies of the atmospheric variability. It is proposed as a dynamics-rooted alternative to the traditional EOF analysis, in so far as its basis functions are chosen to be orthogonal with respect to wave activities.

In nonlinear regimes, the ENM method generates basis functions with a possibly more physical interpretation. The algorithm provides information on the validity of linear ideas, as exemplified by the phase speed comparison in which the mean phase speed obtained from a typically nonmonochromatic power spectrum is compared with the value predicted by the linearized dynamics.

In linear or quasi-linear regimes, such as those produced by linear runs of atmospheric models, the ENM algorithm can provide a valuable alternative to other modal decomposition techniques, which usually begin by deriving the complete set of normal modes and only then project the data. The ENM method directly captures the subset of modes that have actually been excited, with the corresponding amplitudes. Even in situations where less familiar kinds of modes are present, such as quasi modes, the ENM algorithm is seen to be a useful descriptor.

As a first application, we made a diagnostic study of upper-tropospheric and lower-stratospheric winter data taken from NCEP reanalyses. The upper regions were neglected under the assumption that they carry relatively small amounts of wave activity. The boundary layer and the lower troposphere were masked and considered as a means of forcing the upper levels. A complete set of ENMs, orthogonal with respect to the norm defined by pseudomomentum, was constructed for zonal wavenumbers 1 to 9, using the zonal climatology as basic state.

The partition of kinetic and available potential energy of ENMs was shown to depend on both spectral param-

eters, the wavenumber s, and the ENM number n. In the subrange of the leading planetary modes the ratio of kinetic to potential energy gradually goes from approximately 1 to 3, in the wavenumber range considered in this study (i.e., $1 \leq s \leq 9$). Some spectral subranges with intriguing power-law behavior of the type $E \sim n^{-b}$ were observed at all wavenumbers, but a precise explanation of this property is still missing due to the nontrivial relation between the ENM index n and ordinary spatial scales.

We found that the spatial profile of the leading ENMs' wave activity is compatible with previous studies of the zonal wavenumber/latitude distribution of the eddy mean kinetic energy. The leading mode with wavenumber 5, centered in Southern Hemisphere midlatitudes was shown to have characteristics of an upper-tropospheric midlatitude quasi mode propagating with a phase speed of $\sim$12 m s^{-1} and decay rate of $\sim$3 days. We believe this is the first observational detection of upper-tropospheric, large-scale quasi modes in analyzed data.

The average phase speed of other leading modes was compared with values predicted by the linear theory of normal modes with stochastic forcing, showing a good agreement even though the calculation of large periods of modes with small wavenumbers is not so robust as it is with larger wavenumbers. Considering that only 4-month periods of data were taken, one should not expect the ENM analysis in this paper to resolve low-frequency oscillations—say, with periods longer than 2 months. Seasonal cycles and interannual variations are likely to have only a small projection on the large-scale, low-frequency ENMs.

Based on the wave activity spectra shown here, ENMs may seem less capable of concentrating information than are EOFs. Concentration of information is often measured by the variance explained by the leading basis functions. By choosing the variance as a measure—instead of wave activity—EOFs will naturally have the largest reduction power (Brunet and Vautard 1996). However, the leading EOF will probably have projections on many normal modes, which may obscure its dynamical interpretation. A larger number of ENMs may be needed to explain the same amount of variance of a single EOF, but the dynamical properties of each ENM will be better defined.

The use of isentropic coordinates proved convenient in the domain and at the large scales considered in this study. To extend the algorithm to other regions, like the lower troposphere, one should carry out a change of coordinates and redesign the construction of correlation matrices accordingly. The inclusion of boundary effects could also be considered as a way of capturing unstable modes. A nonsymmetric basic state and the associated pseudoenergy norm could also be considered in future versions of the algorithm, and applied to the diagnosis of asymmetric features like the midlatitude storm tracks.

We believe that the algorithm, in its present form, is particularly suitable for studies of the variability in numerical models. For instance, it provides a recipe to characterize the normal modes excited in linear or weakly nonlinear runs. It can also be used in dynamical core experiments as a way of comparing the variability in two different models, or the variability in a single model with different forcings. A diagnostic study of this kind, using the Canadian Global Environmental Multiscale model's dynamical core appears elsewhere (Zadra et al. 2002).

Acknowledgments. The authors wish to thank B. Dugas, N. Gagnon, and M. Charron for help in preparing the data and developing the algorithm. A. Zadra thanks P. Bartello and M. Montgomery for insightful discussions and acknowledges support from the McGill's Faculty of Graduate Studies and Research, the ''Fonds pour la Formation de Chercheurs et l'Aide à la Recherche du Québec,'' and the Meteorological Service of Canada.

REFERENCES

Andrews, D. G., 1983a: A conservation law for small-amplitude quasi-geostrophic disturbances on a zonally asymmetric basic. *J. Atmos. Sci.,* **40,** 85–90.

——, 1983b: A finite-amplitude Eliassen–Palm theorem in isentropic coordinates. *J. Atmos. Sci.,* **40,** 1877–1883.

——, J. R. Holton, and C. B. Leovy, 1987: *Middle Atmosphere Dynamics.* Academic Press, 489 pp.

Boer, G. J., and T. G. Shepherd, 1983: Large-scale two-dimensional turbulence in the atmosphere. *J. Atmos. Sci.,* **40,** 164–184.

Brunet, G., 1994: Empirical normal-mode analysis of atmospheric data. *J. Atmos. Sci.,* **51,** 932–952.

——, and P. H. Haynes, 1996: Low-latitude reflection of Rossby wave trains. *J. Atmos. Sci.,* **53,** 482–496.

——, and R. Vautard, 1996: Empirical normal modes versus empirical orthogonal functions for statistical prediction. *J. Atmos. Sci.,* **53,** 3468–3489.

Charney, J. G., 1971: Geostrophic turbulence. *J. Atmos. Sci.,* **28,** 1087–1095.

Charron, M., and G. Brunet, 1999: Gravity wave diagnosis using empirical normal modes. *J. Atmos. Sci.,* **56,** 2706–2727.

Chen, T. C., M. C. Yen, and D. P. Nune, 1987: Dynamic aspects of the Southern Hemisphere medium-scale waves during the summer season. *J. Meteor. Soc. Japan,* **65,** 401–421.

Eady, E. T., 1949: Long waves and cyclone waves. *Tellus,* **1,** 33–52.

Edouard, S., R. Vautard, and G. Brunet, 1997: On the maintenance of potential vorticity in isentropic coordinates. *Quart. J. Roy. Meteor. Soc.,* **123,** 2069–2094.

Gill, A. E., 1982: *Atmosphere–Ocean Dynamics.* Academic Press, 662 pp.

Green, J. S. A., 1960: A problem in baroclinic instability. *Quart. J. Roy. Meteor. Soc.,* **86,** 237–251.

Haynes, P. H., 1988: Forced, dissipative generalizations of finite-amplitude wave-activity conservation relations for zonal and nonzonal basic flows. *J. Atmos. Sci.,* **45,** 2352–2362.

Held, I. M., 1985: Pseudomomentum and the orthogonality of modes in shear flows. *J. Atmos. Sci.,* **42,** 2280–2288.

Hoskins, B. J., and D. Karoly, 1981: The steady linear response of a spherical atmosphere to thermal and orographic forcing. *J. Atmos. Sci.,* **38,** 1179–1196.

Killworth, P. D., and M. E. McIntyre, 1985: Do Rossby-wave critical layers absorb, reflect or over-reflect? *J. Fluid Mech.,* **161,** 449–492.

Lambert, S., 1986: A study of eddy kinetic energy of the Southern

Hemisphere during january and july with emphasis in the FGGE year. *Tellus*, **38A,** 429–438.
Lin, C. A., and A. C. M. Chan, 1989: Baroclinic instability and the summer Southern Hemisphere wavenumber 5 circulation. *Geophys. Astrophys. Fluid Dyn.*, **47,** 19–42.
Longuet-Higgins, M., 1968: The eigenfunctions of Laplace's tidal equations over a sphere. *Philos. Trans. Roy. Soc. London*, **262A,** 511–607.
Magnusdottir, G., and P. H. Haynes, 1998: Reflection of planetary waves in three-dimensional tropospheric flows. *J. Atmos. Sci.*, **56,** 652–670.
McIntyre, M., and T. Shepherd, 1987: An exact local conservation theorem for finite-amplitude disturbances to non-parallel shear flows, with remarks on Hamiltonian structure and Arnold stability theorems. *J. Fluid Mech.*, **181,** 527–567.
North, G. R., 1984: Empirical orthogonal functions and normal modes. *J. Atmos. Sci.*, **41,** 879–887.
Rivest, C., and B. F. Farrell, 1992: Upper-tropospheric synoptic-scale waves. Part II: Maintenance and excitation of quasi-modes. *J. Atmos. Sci.*, **49,** 2120–2138.
——, C. A. Davis, and B. F. Farrell, 1992: Upper-tropospheric synoptic-scale waves. Part I: Maintenance as Eady normal modes. *J. Atmos. Sci.*, **49,** 2108–2119.
Sirovich, L., and R. Everson, 1992: Management and analysis of large scientific datasets. *Int. J. Supercomp. Appl.*, **6,** 50–68.
Zadra, A., 2000: Empirical normal mode diagnosis of reanalysis data and dynamical-core experiments. Ph.D. thesis, McGill University, 221 pp.
Zadra, A., G. Brunet, J. Derome, and B. Dugas, 2002: Empirical normal mode diagnostic study of the GEM model's dynamical core. *J. Atmos. Sci.*, **59,** 2498–2510.